Seismic risk assessment of a 50 m high masonry chimney using advanced analysis techniques

Fabio Minghini [a,*], Gabriele Milani [b,1], Antonio Tralli [a,2]

[a] Engineering Department, University of Ferrara, Via Saragat 1, 44122 Ferrara, Italy
[b] Department of Architecture, Built Environment & Construction Engineering (ABC), Politecnico di Milano, Piazza Leonardo da Vinci 32, 20133 Milan, Italy

Article history:
Received 17 January 2014
Revised 21 March 2014
Accepted 25 March 2014

1. Introduction

The recent Emilia earthquake sequence was characterized by prevailing low-frequency contents and strong vertical components, that are typical of near-fault seismic events. Therefore, structures having natural periods greater than those of ordinary buildings, such as precast reinforced concrete structures [1] and relatively slender historical masonry constructions, i.e., churches, bell towers and castles [2], suffered from severe damages. In this context, industrial masonry chimneys deserve special attention. In fact, the area along the Po river has historically been the seat of agricultural transformation activities, flourished particularly between the end of the 19th century and the beginning of the 20th century. These plants were typically provided with steam boilers and chimneys, which of course were dismissed starting from the 1950s when electric power replaced steam. As a matter of fact, industrial chimneys nowadays characterize the landscape and belong to the cultural heritage of this region. These structures were shown to be particularly prone to the earthquake effects. A number of masonry chimneys near Ferrara had been so severely damaged that a complete demolishment became necessary for safety reasons.

The existing literature related to the numerical analysis of chimneys is rather scarce. Some recent and insightful 3D nonlinear analyses of a collapsed reinforced concrete chimney were presented in [3,4]. With regard to masonry chimneys, an interesting state-of-the-art review of the construction methods and numerical modeling techniques used for assessing the seismic vulnerability is presented in [5]. In [6,7] a number of linear finite-element analysis results were reported, including the effects due to temperature gradients, wind loading and seismic action. In these papers, some of the issues associated with restoration were also presented. In the field of the analysis of earthquake-induced damages, the higher-mode effects associated with high-frequency content ground motions were pointed out in [8], whereas a typical first-mode failure mechanism was discussed in [9]. Similar aspects were emphasized in [10] using accurate nonlinear finite-element analyses. For the chimney analyzed in that work, collapse was found to be triggered by masonry cracking at the base. In [11], a critical comparison between nonlinear static and dynamic analysis methods is presented with reference to a stone masonry minaret. With regard to the structural characterization of masonry chimneys, an experimentally-based model updating technique is developed in

* Corresponding author. Tel.: +39 (0)532 974912; fax: +39 (0)532 974870.
E-mail addresses: fabio.minghini@unife.it (F. Minghini), milani@stru.polimi.it (G. Milani), antonio.tralli@unife.it (A. Tralli).
[1] Tel.: +39 (0)2 2399 4290; fax: +39 (0)2 2399 4220.
[2] Tel.: +39 (0)532 974822; fax: +39 (0)532 974870.

[12]. Provided that the experimental vibration mode shapes are carefully identified, the obtained updated numerical model takes account of the stiffness variations along the chimney shaft due to possible damages and can profitably be used for assessing the structural stability [13]. An experimentally-calibrated numerical model is used in [14] to verify the effectiveness of the seismic strengthening of an industrial masonry chimney using CFRP strips.

The present paper is devoted to the analysis of a 50 m tall brickwork chimney located in Ferrara (Fig. 1a), i.e., about 30 and 40 km far from the epicenters of the first and second main shocks of Emilia earthquake, respectively (Fig. 2). The chimney was built at the beginning of the 20th century in the service of a sugar factory. Because of the atmospheric agents, the structure is affected by a significant mortar deterioration from a height of approximately 35 m up to the top (Fig. 1b). After Emilia earthquake's main shocks, the chimney showed evident diagonal cracks at an altitude of approximately 46 m (Fig. 3a and b). The principal objective of this investigation is to evaluate the seismic vulnerability of the chimney and to explain the causes of the observed damages. Both linear and nonlinear static and dynamic finite-element models were developed. In particular, modal pushover analysis [16] including six lateral force distributions and nonlinear response history analysis using rigid triangular elements connected to one another by means of specifically developed nonlinear interfaces indicate a strong influence of the higher-mode contributions, in conjunction with material deterioration.

2. Geometrical and mechanical survey

A preliminary survey campaign was aimed at evaluating the chimney's geometry. The thickness (t) was determined at 17 different locations along the shaft by drilling through the masonry wall. For the same cross sections, the outer diameter ($\varnothing_{out}$) was estimated from the measurement of the circumference length. These estimates were confirmed by a 3D laser scanning of the chimney. The results of the geometrical survey are reported in Table 1 in ascending order of the vertical coordinate z originating from the base. For z lying in the range 39–50 m, the masonry wall is constituted by one single course of blocks with a thickness of 0.22 m (fourth column of Table 1). This part of the structure is affected by a significant mortar degradation (Fig. 1b) and earthquake-induced cracks (Fig. 3a and b).

A second survey campaign was carried out to estimate the compressive strength of the masonry units and identify the constituents of the mortar. First, rebound hammer tests were conducted on the outer surfaces of the blocks, showing a substantial response homogeneity from the base to the top of the chimney. Then, six blocks were taken from the structure at $z \geqslant 40$ m (Fig. 3c). A total of 34 compression tests on cubes with edge length of 50 mm (Fig. 3d) obtained from the 6 blocks were conducted in accordance with [17]. Before the tests, the specimens were air-dried to reduce the uncertainties due to their moisture content. The resulting average mass density was approximately 1600 kg/m^3. The mean value of the compressive strength resulted to be 12 MPa. The failure surfaces were generally regular (Fig. 3e), indicating a low percentage of voids. With regard to the mortar, chemical and diffractometric analyses were carried out on three samples, two of which taken at $z = 2$ m and the third at $z = 45$ m. The sand fraction resulted to be quartz-rich and a high gypsum content was observed only for the third sample. Taking account of both degradation and composition variations observed for the mortar, the choice of a mortar strength class M2.5 (see [18]) appears to be reasonable. Hence, on the basis of the mean compressive strength of the blocks $f_{bm} = 12$ MPa obtained from the tests, the Italian Building Code [19] yields a mean compressive strength for the masonry approximately equal to $f_m = 4.2$ MPa. Although no in situ material testing was performed, the described survey is believed to ensure a knowledge level KL2 according to [20], leading to a confidence factor CF = 1.2.

3. Linear elastic analysis

3.1. Vibration frequencies and mode shapes

For the linear analyses, a finite element (FE) model of the chimney was developed using two-node shear deformable beam elements of the STRAND7 element library [21]. In particular, 200 locking-free elements with circular hollow cross section and length 0.25 m were used. The section diameters and thicknesses were given the values determined experimentally. For a review of the locking-free properties of shear deformable beam elements see for example [22]. A lumped formulation was adopted for the mass matrix. Unit weight w and longitudinal and shear elastic moduli E and G used in the analyses are reported in the first three columns of Table 2 [19].

When all degrees of freedom for the node at the base are suppressed (fixed-base case), there are six flexural mode shapes with modal mass not lower than 5% (Fig. 4). The natural vibration frequencies and the corresponding periods, effective modal masses and modal participation factors for these modes are reported in Table 3. In particular, modal participation factor Γ_n and effective modal mass M_n^* for the nth mode are defined as [23]

$$\Gamma_n = L_n / M_n \tag{1}$$

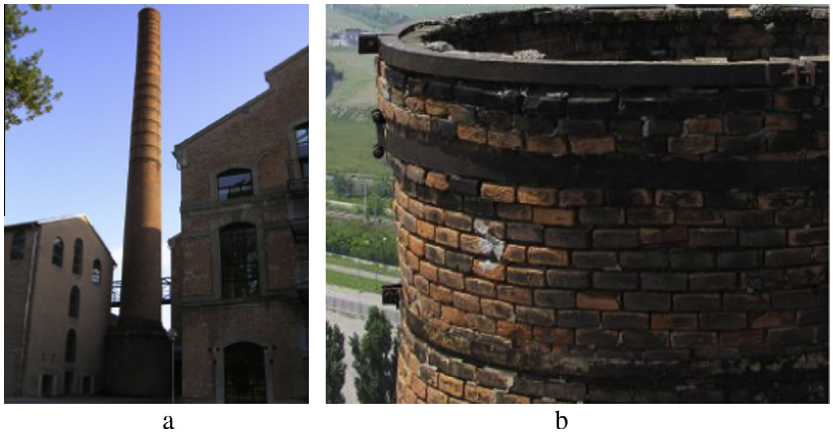

a b

Fig. 1. (a) Lateral view of the chimney; and (b) mortar deterioration in the upper part.

Fig. 2. Satellite map [15] of the Italian region stricken by the 2012 earthquake sequence, showing the location of the chimney and the epicenters of the two main shocks.

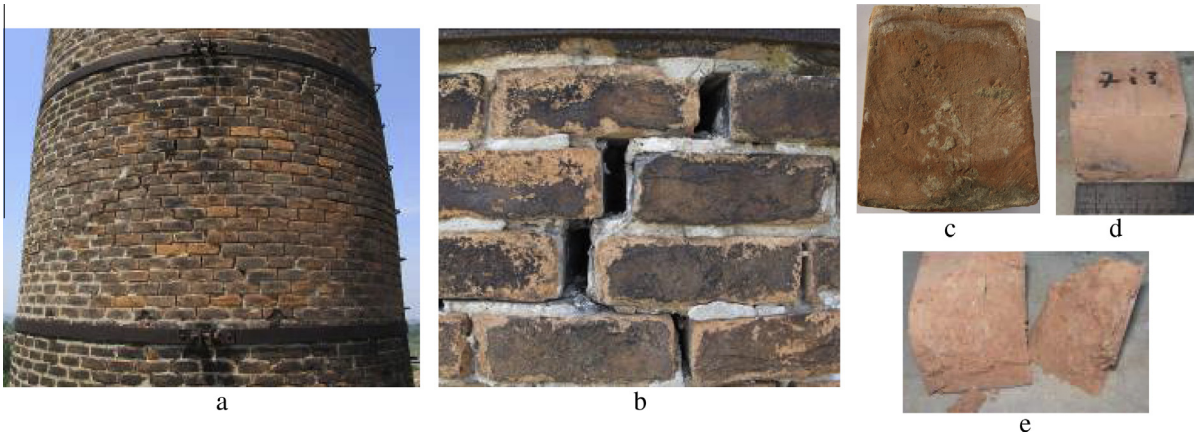

Fig. 3. (a) Diagonal cracks observed after Emilia earthquake's main shocks; (b) detail view of a crack; (c) block taken from the 0.22 m-thick part of the chimney; (d) cubic specimen before and (e) after the compression test.

Table 1
Chimney's geometry.

Investigated section	Position along the vertical axis, z (m)	Outer diameter, ϕ_{out} (m)	Wall thickness, t (m)
S1	1.5	6.50	1.82
S2	7.3	4.73	0.95
S3	10.6	4.62	0.95
S4	11.0	4.60	0.50
S5	11.6	4.58	0.28
S6	12.0	4.56	0.28
S7	16.0	4.42	0.28
S8	20.0	4.27	0.28
S9	25.0	4.09	0.28
S10	30.0	3.91	0.28
S11	35.0	3.73	0.28
S12	38.4	3.60	0.28
S13	39.2	3.59	0.22
S14	40.0	3.55	0.22
S15	45.0	3.36	0.22
S16	48.0	3.25	0.22
S17	50.0	3.18	0.22

Table 2
Material properties used in the linear analyses.

Specific weight w (kN/m^3)	Elastic moduli		Compressive strength f_d (MPa)	Shear strength (cohesion) τ_0 (MPa)
	E (MPa)	G (MPa)		
18	1500	500	0.9	0, 0.1, 0.2

$$M_n^* = L_n \Gamma_n = L_n^2 / M_n \tag{2}$$

where $L_n = \boldsymbol{\phi}_n^T \mathbf{M} \boldsymbol{\iota}$, $M_n = \boldsymbol{\phi}_n^T \mathbf{M} \boldsymbol{\phi}_n$ and $\boldsymbol{\phi}_n$, $\mathbf{M}$ and $\boldsymbol{\iota}$ are the nth eigenvector, the global mass matrix and the influence vector, respectively. Each element of vector $\boldsymbol{\iota}$ is equal to 1. It can be noted that the modal mass of the first mode is only 22% of the total mass. The sum of the six modal masses is approximately equal to 71% of the total mass.

For slender structures such as chimneys and towers, the soil-structure interaction effects in the presence of earthquake loading may be relevant [24] and their quantification should be based on extensive in situ investigations [25]. To account for the effects of

Table 3
Results of the frequency analysis considering and neglecting the soil-structure interaction (SSI) for the six mode shapes of Fig. 4.

Mode	SSI not included				SSI included	Percentage difference
	Frequency, f_i (Hz)	Period, T_n (s)	Effective modal mass/total mass, M_n^*/M (%)	Participation factor, Γ_n	Frequency, $f_{i,SSI}$ (Hz)	$100 \times \lvert f_{i,SSI} - f_i \rvert / f_i$ (%)
1	0.51	1.95	22.0	1.74	0.51	0.33
2	2.47	0.41	11.5	1.32	2.45	0.77
3	6.01	0.17	10.9	1.28	5.89	2.03
5	10.42	0.10	13.1	1.27	9.99	4.09
6	15.96	0.06	8.8	1.14	15.29	4.20
8	23.51	0.04	5.0	0.86	22.49	4.34
Total activated mass			71.3			

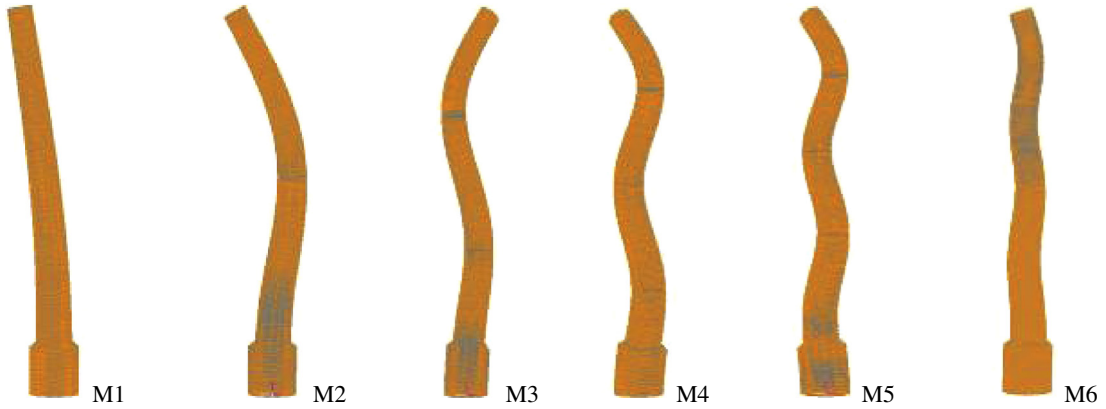

Fig. 4. Mode shapes corresponding to the natural frequencies reported in Table 3.

the soil-structure interaction, the formulation outlined in [26] for rigid massless foundations was adopted, leading to the following general expression for the dynamic stiffness of the foundation:

$$K^d = K^s(k + ia_0c) \tag{3}$$

where K^s is the static stiffness and the terms in parentheses include the dynamic contribution. In Eq. (3), i is the imaginary unit, whereas $a_0 = \omega R/V_s$ represents the nondimensional frequency, with ω, R and V_s being the angular frequency of the motion, the foundation radius and the shear wave velocity in the soil, respectively. Finally, k and c are frequency-dependent functions typically referred to as stiffness and damping coefficient, respectively. With reference to the horizontal (index "H") and rocking (index "R") modes of cylindrical embedded foundations, neglecting the damping term, the dynamic stiffnesses may be written as [27]

$$K_H^d = K_H^s k_H = 8GR(1 - h_f/R)/(2 - \nu) \tag{4}$$

$$\begin{aligned} K_R^d &= K_R^s k_R \\ &= 8GR^3[1 + 2.3h_f/R + 0.58(h_f/R)^3] \\ &\quad \times [1 - 0.35a_0^2/(1 + a_0^2)]/[3(1 - \nu)] \end{aligned} \tag{5}$$

where G and ν are shear modulus and Poisson's ratio of the soil, respectively, whereas h_f represents the depth of embedment. For this particular case only the rocking stiffness turns out to be frequency-dependent (Eq. (5)). In fact, in Eq. (4), the stiffness coefficient $k_H = 1$ makes the horizontal stiffness coincide with the corresponding static contribution. The soil underlying the chimney may realistically be considered to be compact because of the sustained vertical load. Hence, for the shear modulus, the value $G = 0.25$ GPa was considered to be suitable. Moreover, by assuming soil mass density and Poisson's ratio to be given by $\rho = 1950$ kg/m^3 and $\nu = 0.25$, respectively, estimating the shear wave velocity with the usual relation $V_s = (G/\rho)^{0.5}$ and taking account of the geometric quantities $R = 3.75$ m and $h_f/R = 1.8$ yield the foundation stiffnesses $K_H^d = 1.23 \times 10^{10}$ N/m and $K_R^d = (4.25 \times 10^{11})(9116.8 + 0.65\omega^2)/(9116.8 + \omega^2)$ N m. For the purpose of comparison with the fixed-base case, the rocking stiffness was approximated by the weighted mean value $K_{Rm}^d = 2.82 \times 10^{11}$ N m, obtained using the effective modal masses of Table 3 as the weights. The natural frequencies for the mode shapes of Fig. 4 evaluated by including the soil-structure interaction are reported in the sixth column of Table 3. The minimum and maximum (absolute) values of the difference with respect to the fixed-base case are only 0.33% and 4.34%, and correspond to the fundamental and the eighth modes, respectively (last column of Table 3). Hence, to a first approximation, the soil-structure interaction can be neglected in this special situation and only the fixed-base case will then be considered in the following.

3.2. Linear static analysis

In the framework of the linear seismic analysis of slender structures belonging to the cultural heritage, the Italian Guideline [28] allows for the use of the lateral force method [29]. Therefore, a distribution of horizontal nodal forces proportional to m_iz_i was applied to the FE model described in the previous section, with m_i and z_i being the mass and the height above the soil surface, respectively, referred to the ith node of the mesh. The resultant of the lateral force distribution was assumed to be $F_h = 0.85S_e(T_1)W/(qg)$ where $S_e(T_1)$ is the ordinate of the elastic response spectrum given by [19] in correspondence of the fundamental period $T_1 = 1.95$ s

(Table 3), W is the self weight of the chimney, g is the standard gravity and $q = 2.8$ is the behavior factor suggested by [28] in the case of slender structures with sudden stiffness changes in elevation. Coefficient 0.85 accounts for the reduction in the effective mass of the fundamental mode with respect to the low-rise buildings. The available estimates of the shear wave velocity indicate an intermediate soil site class between ground types C and D, see [19,29]. Furthermore, in accordance with the definition of the return period for the seismic action reported in [19], a suitable use class should be chosen for the chimney. In this case, the choice of the use class is driven by the use classes of the buildings that rise in the surrounding area, including both offices (use class II) and university classrooms (use class III). Hence, with the purpose of a parametric analysis, ground types C and D and use classes II and III were alternatively considered in evaluating $S_e(T_1)$ (Table 4). However, for the sake of brevity, only the results corresponding to use class II and ground type C are presented in the following.

The ratio $e_{LFM} = M_{Ed,LFM}/N_{Ed}$ between the bending moment $M_{Ed,LFM}$ obtained from the lateral force method and the axial load N_{Ed} is reported in Fig. 5a versus z (dashed line). In the same figure, the solid line represents the outer radius of the chimney. The distance between the two curves attains its minimum for the cross section located at approximately $z = 11$ m, corresponding to the change in thickness from 0.5 m to 0.28 m (Table 1).

3.3. Modal response spectrum analysis

The modal response spectrum analysis was performed by applying the Complete Quadratic Combination (CQC) rule to the effects of the first 12 modes of vibration, including the six modes of Fig. 4. The activated mass reaches, thereby, about 80% of the overall mass. In analogy with the static analysis, a behavior factor $q = 2.8$, use class II and ground type C were assumed. The ratio $e_{RSM} = M_{Ed,RSM}/N_{Ed}$ between the bending moment $M_{Ed,RSM}$ obtained from the response spectrum method and the axial load N_{Ed} is reported in Fig. 5a versus z (dotted line). Because of the effects due to the modes higher than the fundamental mode, e_{RSM} tends to approach the outer radius especially for z lying in the range 40–45 m and crosses the curve of the static analysis for $z = 34$ m.

Table 4
Seismic parameters used to define the horizontal-elastic acceleration response spectra for the site [19].

Use class	T_R[a] (years)	a_g[b]/g	F_0[c]	T_C^*[d] (s)	S[e] Ground type	
					C	D
II	475	0.137	2.594	0.273	1.488	1.800
III	712	0.162	2.567	0.276	1.451	1.778

[a] T_R = return period.
[b] a_g = design ground acceleration on type A ground.
[c] F_0 = maximum spectral amplification factor.
[d] T_C^* = period defining the beginning of the constant velocity range of the spectrum.
[e] S = soil factor.

3.4. ULS verification for bending and shear

Although the masonry compressive strength was estimated from the mechanical survey, for the preliminary safety verification for bending presented in this section the recommendations reported in [19] for low-quality masonry and knowledge level KL2 were followed. Then, the masonry compressive strength was conservatively assumed to be $f_d = f_m/(CF\gamma_m) = 0.9$ MPa (Table 2), with $f_m = 2.2$ MPa and $\gamma_m = 2$ being the mean masonry compressive strength and the partial safety factor provided by the Italian Building Code [19]. For no-tension beams, the moment resistance for the generic cross section is usually evaluated as $M_{Rd} = N_{Ed}h_0$, with N_{Ed} and h_0 being the local value of the axial load and the distance between the cross section centroid and the point of application of the compressive stress resultant, respectively. The distribution of the compressive stresses over the cross section was approximated by a stress block with effective strength equal to $0.85f_d = 0.79$ MPa [19]. The depth of the stress block was evaluated by imposing the equilibrium along the vertical direction. The bending moment diagrams $M_{Ed,LFM}(z)$, $M_{Ed,RSM}(z)$ obtained from the linear analyses are compared in Fig. 5b with $M_{Rd}(z)$. For $z = 11$ m, in accordance with the maximum in the eccentricity plot of Fig. 5a, the value of $M_{Ed,LFM}$ given by the static analysis significantly exceeds the moment resistance, indicating a failure mode by overturning at that section. The Peak Ground Acceleration (PGA) leading the chimney to collapse is approximately $a_{ULS} = 0.08g$, a value slightly lower than the PGA attained during the Emilia earthquake's main shocks. However, the failure mode by overturning is not confirmed by the observed damages at all (Fig. 3a and b). In contrast, the bending moment obtained from the dynamic analysis is lower than the moment resistance at any given z (Fig. 5b).

With regard to the safety verification for shear, in the absence of a shear failure criterion by diagonal cracking suitable for slender masonry members with annular cross section, the shear resistance was estimated using a sliding shear failure criterion based on the classical Coulomb friction law with friction coefficient $\mu = 0.4$ [18]. In particular, with the aim of a parametric analysis of the shear resistance, three values of the masonry shear strength under zero compressive stress, i.e., $\tau_0 = 0$, 0.1 and 0.2 MPa, were alternatively considered (Table 2). The limiting assumption of zero cohesion seems to be reasonable for the cross sections at $z \geqslant 35$ m, affected by a significant mortar degradation. To define the neutral axis

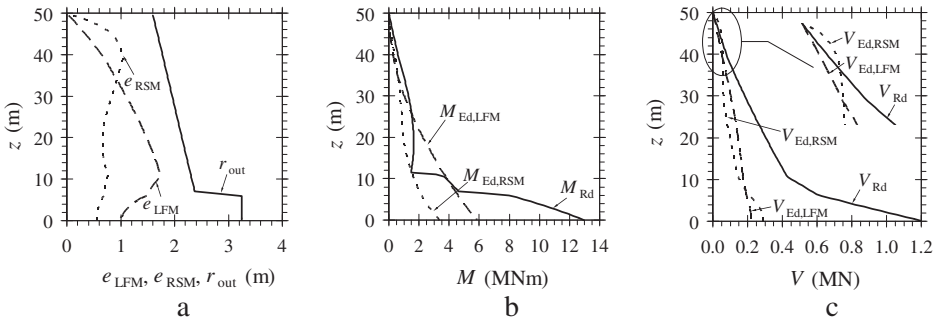

Fig. 5. Linear analyses results: (a) eccentricities obtained from lateral force method (e_{LFM}) and response spectrum method (e_{RSM}) compared with the outer radius of the chimney (r_{out}); (b) FE computed bending moment diagrams ($M_{Ed,LFM}$, $M_{Ed,RSM}$) and moment resistance (M_{Rd}); and (c) FE computed shear force diagrams ($V_{Ed,LFM}$, $V_{Ed,RSM}$) and shear resistance (V_{Rd}) for zero cohesion ($\tau_0 = 0$).

depth, a linear distribution of the compressive stresses over the cross section was assumed (see [18]). The resulting shear resistance is given by $V_{Rd} = l_m t(\tau_0 + 0.4\sigma_n)/\gamma_m$, where $l_m t$ is the area of the part of the cross section in compression; and $\sigma_n = N_{Ed}/(l_m t)$ is the mean compressive stress over the area $l_m t$. The shear force diagrams $V_{Ed,LFM}(z)$, $V_{Ed,RSM}(z)$ obtained from the linear analyses are compared in Fig. 5c with $V_{Rd}(z)$ evaluated for $\tau_0 = 0$. In this case, although the two methods yield in general different values of $l_m t$ for a given z, the curve of the shear resistance turns out to be unique. For the lateral force method, the condition $V_{Ed,LFM} < V_{Rd}$ holds for all z (strictly speaking, V_{Rd} cannot be defined for z lying in the range 10–25 m, where bending failure occurs). In contrast, because of the higher mode contributions, $V_{Ed,RSM}$ exceeds V_{Rd} for $z \geqslant 44$ m, where the compressive stresses are relatively low. The PGA associated with the shear failure mechanism is approximately $a_{ULS} = 0.05g$. Therefore, at least from a qualitative point of view, the dynamic analysis seems to explain the observed damages. If the cohesion is assumed to be $\tau_0 = 0.1$ MPa, no shear failure is encountered.

4. Pushover analysis

4.1. Numerical model

The FE model adopted for the pushover analyses was implemented in DIANA [30] using brick elements. A number of convergence rate tests was conducted to define the mesh size. In particular, 100 and 16 equal subdivisions along the chimney vertical axis and in the planes of the cross sections, respectively, were used, resulting in a total of 1600 brick elements. A preliminary frequency analysis confirmed the results of the beam model described above. The material nonlinearities were reproduced by means of a multi-directional fixed crack model, belonging to the family of the smeared crack constitutive laws [31]. Although this model is specifically suited for concrete, its use for reproducing the nonlinear behavior of masonry was shown to be justified [9,32]. In this case, in order to better approximate the earthquake resistance of the chimney, the partial factor $\gamma_m = 1$ was used to define the masonry strengths. Moreover, the compressive strength was estimated using the mean value $f_m = 4.2$ MPa obtained from the tests on the masonry units, leading to $f_d = f_m/\mathrm{CF} = 3.5$ MPa. The effects due to cracking were taken into account by using a linear cutoff in the biaxial stress field (σ_1, σ_2), a linear softening for the stress–strain relationship in tension, and, finally, a reduction of the shear stiffness through the shear retention factor $\beta = 0.3$. The model parameters are summarized in Table 5.

4.2. Analyses using classical force distributions

Four lateral load distributions commonly used in the pushover analysis are plotted in Fig. 6a against z. Curve $\Phi 1$ is proportional to the fundamental mode (mode $M1$ in Fig. 4); curve M is mass-proportional; curve *LIN* was assumed to vary linearly from the base to the top of the chimney; and, finally, curve *CQC* corresponds to forces F_i proportional to $(V_{Ed,i} - V_{Ed,i+1})$ [33], with $V_{Ed,i}$ and $V_{Ed,i+1}$ being the shear forces obtained from the response spectrum method via CQC rule for the cross sections located at z_i and z_{i+1} ($i = 1, \ldots, n$, with $n = 100$ number of subdivisions along the z-axis

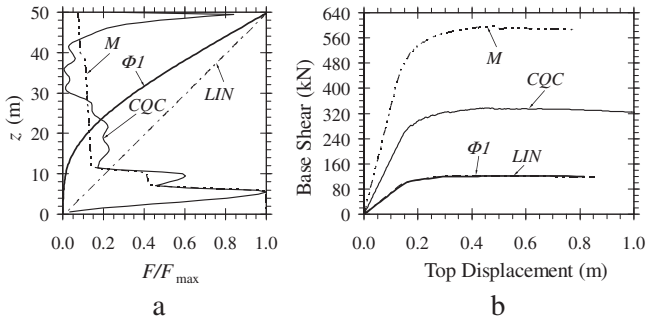

Fig. 6. (a) Traditional lateral load patterns for pushover analysis; and (b) pushover curves for the four load distributions.

used in the FE model). In particular, this force distribution is used to reproduce the shear force diagram given by the linear dynamic analysis. The lateral loads were reproduced by body forces applied to the FE mesh. The corresponding plots of the total base shear versus the horizontal displacement of one of the nodes located at $z = 50$ m are reported in Fig. 6b. As noticed recently in [11] with regard to a 70 m-tall stone masonry minaret, the pushover curves are strongly influenced by the choice of the lateral force distribution. As a matter of fact, using the mass-proportional load pattern yields a maximum base shear force of 600 kN (i.e., about the 10% of the self weight) slightly lower than twice and approximately equal to five times the base shear forces obtained with load patterns *CQC* and $\phi 1$, respectively. Hence, distributions $\phi 1$ and *LIN*, that yield almost coincident pushover curves, resulted to be too conservative. The crack patterns triggered by the four force distributions are shown in Fig. 7a. The widest cracked zone is associated with distribution *CQC*, but all damage patterns substantially indicate the cracking originates at $z = 7$–11 m in correspondence of the first two thickness changes (Table 1) and at those cross sections the chimney collapses by prevailing bending failure. This type of damage was not detected during the post-earthquake survey.

4.3. Modal pushover analysis

The modal pushover analysis (MPA) was introduced in [16] for multistorey framed structures to improve the pushover methods based on force distributions proportional to one single mode of vibration. In that work it was shown that for elastic buildings the MPA procedure coincides with the modal response spectrum method. The basic idea of MPA is to combine (using for example the SRSS rule) the results of N pushover analyses, the nth of which is based on the invariant force distribution proportional to $\mathbf{s}_n^* = \mathbf{M}\boldsymbol{\phi}_n$, with $\boldsymbol{\phi}_n$ being the nth elastic mode shape. The choice of the number N should obviously be governed by the amount of activated mass. In the nth analysis, the structure is pushed to the top displacement

$$u_{tn0} = \Gamma_n \phi_{tn} D_n \tag{6}$$

where Γ_n is defined by Eq. (1), ϕ_{tn} is the component of eigenvector $\boldsymbol{\phi}_n$ corresponding to the monitored node on the top, and D_n represents the peak response for the nth mode SDOF system, obtained from the inelastic response spectrum. Indicating with $\mu_n = D_{nu}/D_{ny}$

Table 5
Material properties used in the pushover analyses.

Young's modulus	Poisson's ratio	Strengths		Ultimate tensile strain	Shear retention factor
		Compressive	Tensile		
E (MPa)	ν	f_c (MPa)	f_t (MPa)	ε_t (‰)	β
1500	0.15	3.5	0.1	0.33	0.3

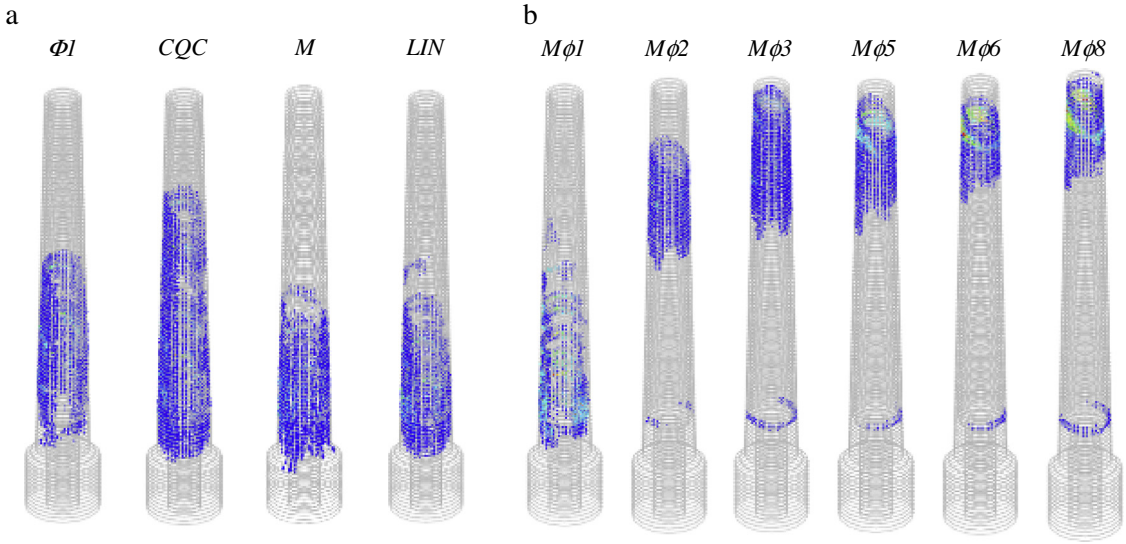

Fig. 7. Damage patterns obtained from (a) pushover analyses using traditional force distributions and (b) modal pushover analysis.

the ductility, i.e., the ratio between ultimate and yielding responses of the nth mode SDOF system, and with $q_n = A_{ne}/A_{ny}$ the nth behavior factor, with A_{ny} and A_{ne} being the maximum pseudo-accelerations for the inelastic and the equivalent elastic systems, respectively, the peak response D_n may be written as [23]

$$D_n = (\mu_n/q_n)(T_n^*/2\pi)^2 A_n \tag{7}$$

In Eq. (7), $T_n^* = 2\pi\sqrt{L_n/k_n^*}$ is the elastic period of vibration of the nth inelastic system, whereas $k_n{}^*$ indicates its elastic stiffness. Although the superposition of uncoupled modal responses has no physical meaning in MDOF inelastic systems, the MPA procedure was shown to perform significantly better than traditional pushover procedures in evaluating story drifts, plastic hinge rotations [34] and member forces [35] for framed structures. Then, in [36,37], the MPA method was extended to the 3D analysis of tall frames including two components of the ground motion. In the case of high-rise cantilevers made of no-tension materials, the MPA is not able to capture the change of the dynamic behavior occurring during the seismic event and can lead to underestimates of the roof lateral displacements [11]. An adaptive pushover method [38] could in theory be used to improve the analysis (see for example [39]), but at the cost of a higher, and often impractical, computational effort. In the present work, the MPA procedure was essentially used to estimate the behavior factor to be introduced into the linear analyses and evaluate the influence of the higher modes on the seismic damage. Six force distributions of the shape $\mathbf{s}_n{}^* = \mathbf{M}\boldsymbol{\phi}_n$ were used (Fig. 8a), where vectors $\boldsymbol{\phi}_n$ (n = 1, 2, 3, 5, 6, 8) are the vibration mode shapes shown in Fig. 4. Because of the irregular mass distribution, load profiles $\mathbf{s}_3^*$ and $\mathbf{s}_5^*$, $\mathbf{s}_6^*$, $\mathbf{s}_8^*$ have their maximum located at z = 7 and 11 m, respectively. Anyway, these profiles significantly stress the chimney in the interval z = 38–43 m. The peak responses D_n obtained from Eq. (7) substantially resulted to be coincident with those obtained from the elastic response spectrum in correspondence of the periods $T_n{}^*$. These displacements are put in evidence in Fig. 8b on the elastic displacement response spectrum given by [19]. The six pushover curves are reported in Fig. 8c, where symbols • refer to the target displacements u_{tn0} given by Eq. (6). With the exception of the curves associated with modes 1 and 2, the target displacements lie on the elastic branch of the curves. Hence, the behavior factors for modes 3, 5, 6 and 8 are equal to unity. For the first two modes the factors q_1 = 1.16 and q_2 = 1.31 were found. The weighted mean value of the behavior factor, with the effective modal masses being the weights, is q = 1.1, in line with the value q = 1.5 recommended in [40] for new masonry chimneys. Then, the above-presented linear analyses should be updated in view of a significantly low dissipative capacity of the chimney.

For a given z, bending moment M_{Ed} and shear force V_{Ed} were obtained from the MPA by integrating the FE computed stresses over the cross section. Moreover, a stress block with effective strength f_d = 3.5 MPa and zero tensile strength were adopted to estimate the moment resistance M_{Rd}. Finally, the relation $V_{Rd} = l_m t(\tau_0 + 0.4\sigma_n)$ was used to approximate the shear resistance. Eccentricity $e = M_{Ed}/N_{Ed}$, bending moment and shear force are compared in Fig. 9a–c with outer radius, bending resistance and shear

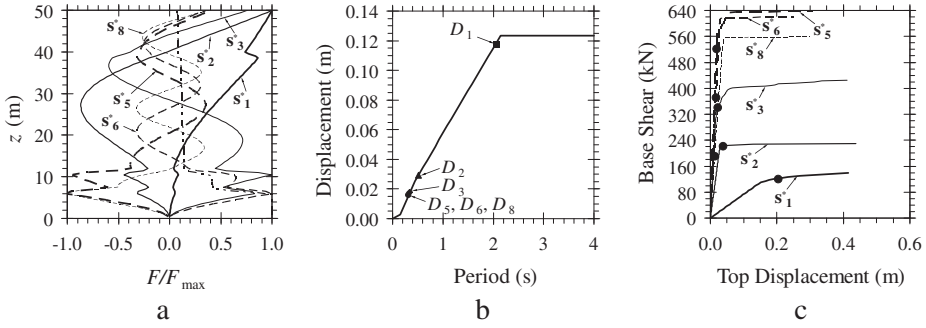

Fig. 8. (a) Lateral load patterns used for the MPA; (b) peak responses for the six SDOF systems reported on the displacement response spectrum given by [19]; and (c) pushover curves for the MPA and corresponding target displacements (symbols •).

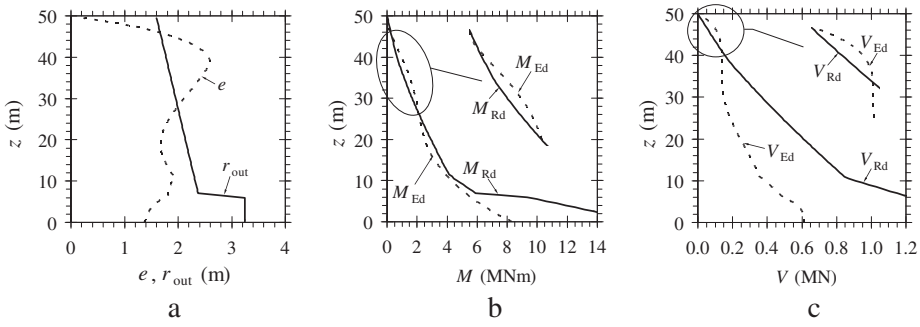

Fig. 9. Modal pushover analysis (MPA) results: (a) eccentricity (e) compared with the outer radius of the chimney (r_{out}); (b) FE computed bending moment diagram (M_{Ed}) and moment resistance (M_{Rd}); and (c) FE computed shear force diagram (V_{Ed}) and shear resistance (V_{Rd}) for zero cohesion ($\tau_0 = 0$).

resistance for zero cohesion ($\tau_0 = 0$), respectively. For 28 m $\leqslant z <$ 46 m, $e > r_{out}$ (Fig. 9a) and $M_{Ed} > M_{Rd}$ (Fig. 9b). Moreover, for $z \geqslant$ 42 m, $V_{Ed} > V_{Rd}$ (Fig. 9c). By assuming $\tau_0 = 0.1$ MPa, the shear failure takes place for $z \geqslant$ 45 m. Therefore, the MPA indicates the chimney is possibly going to collapse in bending at cross sections located at z values significantly higher than predicted by the lateral force method and confirms the shear failure mechanism may be crucial for $z >$ 40 m. These aspects are emphasized by the crack patterns reported in Fig. 7b.

5. Nonlinear response history analysis

A nonlinear response history analysis (RHA) is definitely the most appropriate non-standard numerical procedure to evaluate the actual behavior of a masonry structure during earthquake excitation. Unfortunately, at present, no commercially available software is suitable for reproducing the various constitutive aspects of masonry in the dynamic field. Hence, in the present paper, a numerical model using two-dimensional triangular finite elements specifically developed for the RHA of masonry structures was implemented (Fig. 10). This approach is particularly suited for macro-scale applications where the nonlinear and damaging material response must be defined with satisfactory accuracy using a rather coarse discretization. For comparison purposes, a nonlinear 1D (beam) model of the chimney was also implemented using a commercial software package [21].

5.1. Numerical model

To reproduce the actual geometry (Table 1, Fig. 11a and b), diameter and thickness of the chimney were approximated by piecewise constant functions, yielding 6 different segments with constant annular cross section. These segments were discretized using the three-node elements of Fig. 10. A preliminary convergence rate test was carried out to define the number of subdivisions within the 6 cross sections. The finite element thicknesses were defined by minimizing the difference between the cross sectional second moment of area for each segment of the numerical model and the mean value of the second moment of area for the cross sections of the corresponding actual chimney segment (Table 6). The resulting FE mesh, containing 1562 triangular elements, is shown in Fig. 11c and d. In particular, 24 and 20 subdivisions were used for the cross sections of segments C1 and C2 and for those of segments C3 to C6, respectively.

The finite elements (Fig. 10) were assumed to be rigid and were connected with one another by means of deformable interfaces [41–43]. The interface deformability was reproduced by means of nonlinear normal and tangential springs located at the nodes of the FE mesh (Fig. 10c). Using this approach, full nonlinear analyses of anisotropic materials may be handled by setting ad-hoc interface constitutive laws. In this work, in order to reduce the computational effort, the normal and tangential spring stiffnesses were considered to be uncoupled. Nevertheless, in previously published works (see [43]), this choice was proved to yield accurate predictions of the failure modes.

5.2. Micro-mechanical modeling and homogenization problem

The constitutive laws used for reproducing the behavior of masonry at the macro-scale were defined by solving a homogenization problem at the micro-scale. In particular, a Representative Element of Volume (REV) constituted by 1 brick and 4 fourths, and by the relevant mortar joints, was considered (Fig. 12). The REV was

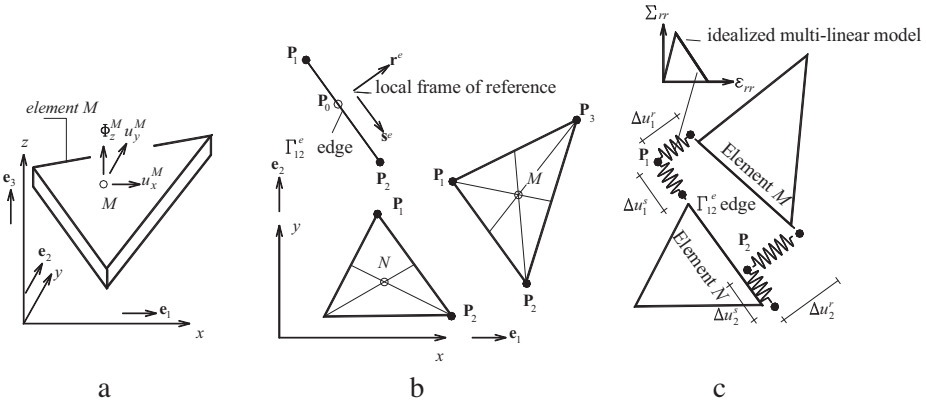

Fig. 10. Rigid triangular element used for the nonlinear dynamic analyses: (a) global optimization unknowns; (b) local axes referred to edge P_1–P_2 between two contiguous elements; and (c) normal and tangential springs at nodes P_1 and P_2 used to define the nonlinear behavior of the interface.

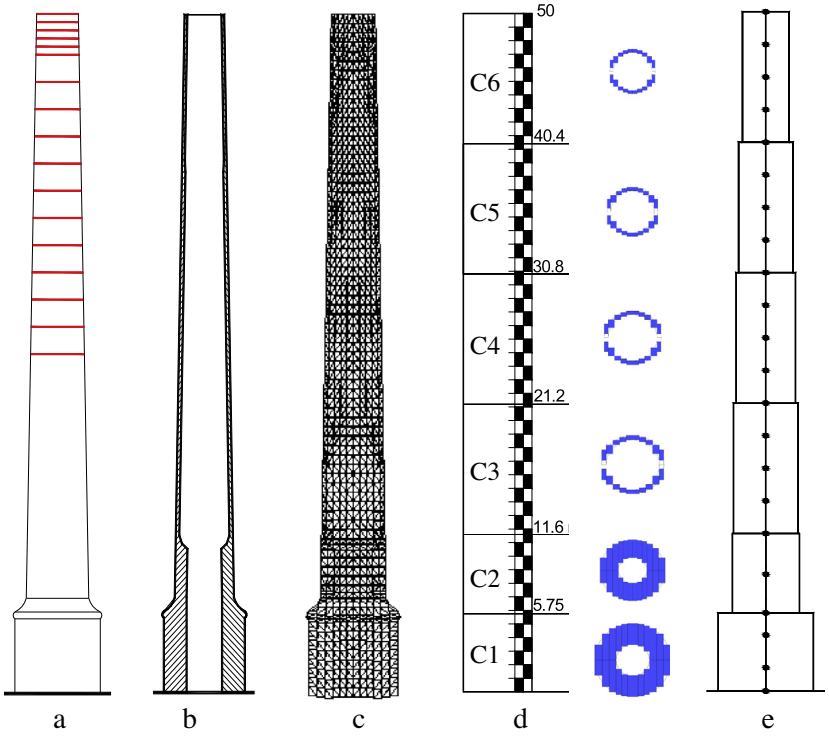

Fig. 11. FE approximations adopted for the RHA: (a) side view and (b) vertical section of the actual chimney; (c) side view of the model using 1562 triangular elements connected through nonlinear interfaces (2D model); (d) segments and corresponding cross sections defined in the 2D model; and (e) side view of the model using 21 nonlinear beam elements (1D model). Blue rectangles in the cross sections of (d) represent the thicknesses of the triangular finite elements. (For interpretation of the references to color in this figure legend, the reader is referred to the web version of this article.)

Table 6
Values of the second moment of area for the 6 cross sections of Fig. 11d compared with the real values.

Second moment of area of the annular cross section (m^4)	Segment					
	C1	C2	C3	C4	C5	C6
Actual geometry[a]	84.38	20.78	7.73	5.92	4.43	2.24
FE model	86.29	21.81	7.94	6.09	4.41	2.30

[a] Mean values within the chimney segments shown in Fig. 11d.

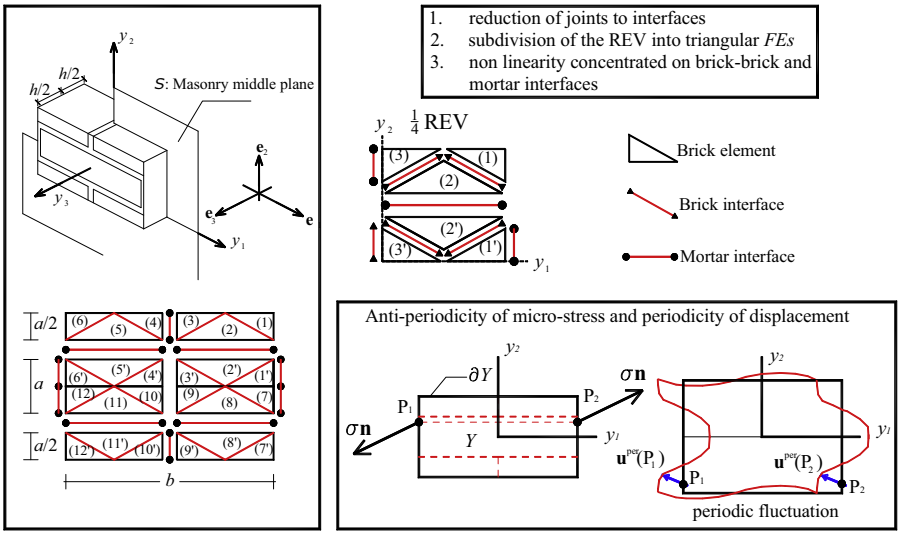

Fig. 12. Micro-mechanical modeling of the REV using 24 triangular elastic elements connected through nonlinear interfaces and anti-periodicity of the micro-stress field [44].

meshed using 24 three-node elastic triangular elements connected with one another by means of nonlinear interfaces. Two different types of interface were used, i.e., interfaces connecting elements that belong to the same brick (referred to as brick interfaces in Fig. 12), and interfaces connecting elements that belong to different bricks through the mortar joint (referred to as mortar interfaces in Fig. 12). Actually, the nonlinear behavior of the REV is ruled by the mortar interfaces, that typically show limiting strengths lower than those of the brick interfaces. The elastic domain of the (mortar) interfaces was considered to be bounded by a composite yield surface that includes tension, shear and compression failure. A multi-surface plasticity model was used, with both tension and compression softening. Finally, the REV was alternatively subjected to in-plane normal and tangential stress distributions, that were applied incrementally. The solutions to these incremental boundary value problems define the nonlinear behavior of the REV. Full details of the procedure may be found in [44,45], where the reader is referred to for further information. Only a brief description of the non-standard yield surfaces adopted for tension and shear behavior of the interfaces is reported hereinafter, whereas, with regard to the nonlinear behavior of the interfaces in compression, the formulation proposed by Lourenço and Rots [46] was adopted.

For both tension and shear failure modes, an associated flow rule was used. With regard to the tension failure mode, the yield function was assumed to be of the following form:

$$f_1(\boldsymbol{\sigma}, \kappa_1) = \sigma - f_t(\kappa_1) \tag{8}$$

with $\boldsymbol{\sigma} = [\sigma, \tau]^T$ being the vector collecting the in-plane stress components acting on the REV, i.e., the normal stress σ and the shear stress τ. Parameter f_t in Eq. (8) indicates the normal stress

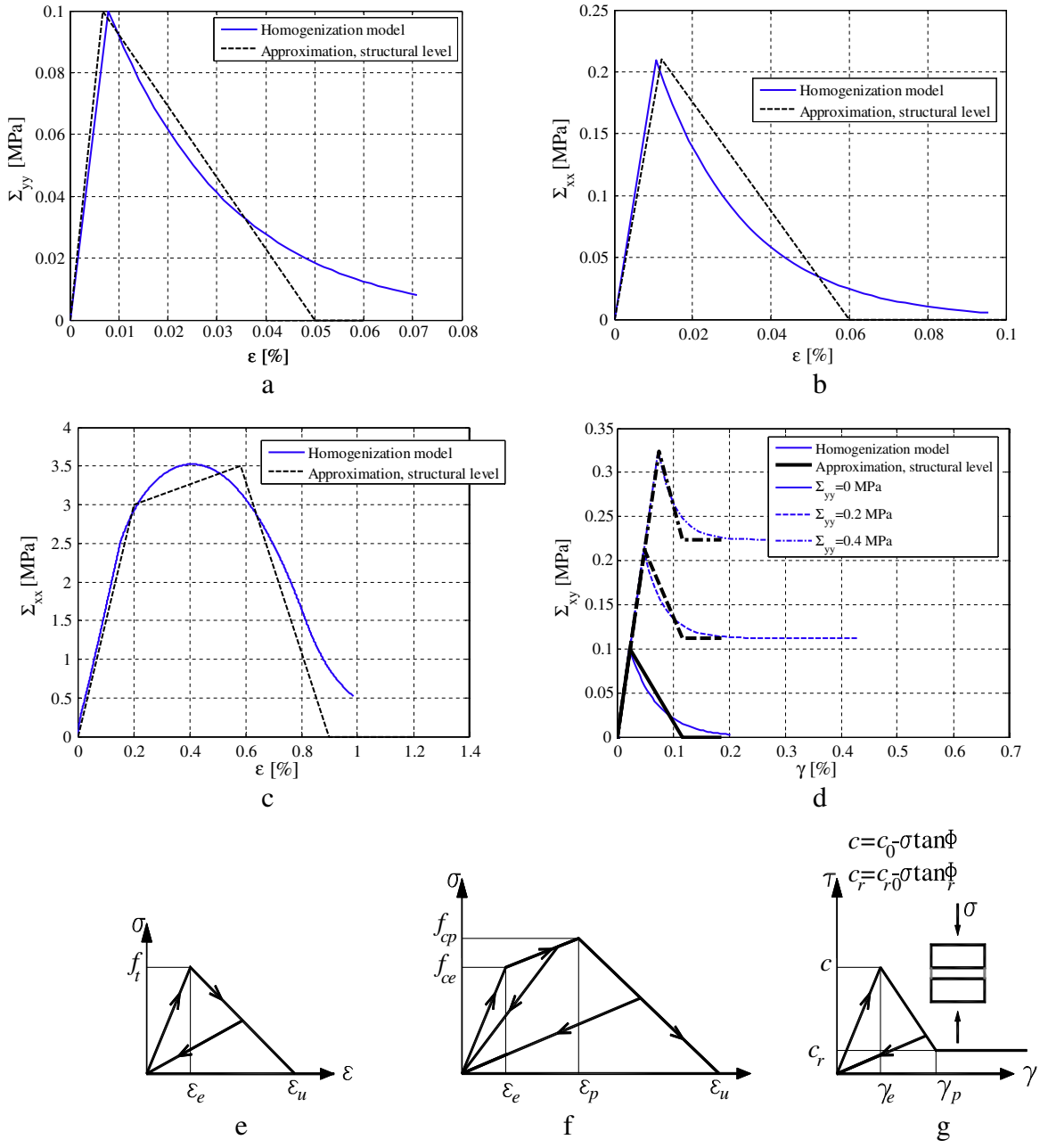

Fig. 13. Comparison between homogenized behavior (blue lines) of the mortar interfaces and multi-linear approximations (black lines): tensile behavior for (a) horizontal and (b) vertical interfaces; (c) compressive behavior; and (d) shear behavior for different values of the compression stress. Cyclic stress–strain relationships for the springs used to reproduce the interface deformability: (e) tensile behavior; (f) compressive behavior; and (g) shear behavior. (For interpretation of the references to color in this figure legend, the reader is referred to the web version of this article.)

corresponding to the attainment of the yield surface in tension. According to the available experimental results on Mode-I failure [46], an exponential softening law was assumed for f_t, yielding the equation:

$$f_t(\kappa_1) = f_{t0} \exp\left(-\kappa_1 f_{t0}/G_f^I\right) \tag{9}$$

with f_{t0} and G_f^I being initial tensile strength of the interface and Mode-I fracture energy, respectively. With regard to the shear failure mode, the yield function was assumed to be of the following form:

$$f_2(\boldsymbol{\sigma}, \kappa_2) = |\tau| + \sigma \tan\phi(\kappa_2) - c(\kappa_2) \tag{10}$$

Functions c and $\tan\phi$ in Eq. (10), that represent cohesion and friction coefficient corresponding to the attainment of the yield surface in shear, are given by the following expressions:

$$c(\kappa_2) = c_0 \exp(-\kappa_2 c_0/G_f^{II}) \tag{11}$$

$$\tan\phi(\kappa_2) = \tan\phi_0 + (\tan\phi_r - \tan\phi_0)(c_0 - c)/c_0 \tag{12}$$

with $\tan\phi_0$, $\tan\phi_r$, c_0, and G_f^{II} being initial and residual friction coefficients, initial cohesion and Mode-II fracture energy, respectively. Parameters κ_1 and κ_2 in Eqs. (8)–(12) are non-negative scalars used to define the equivalent plastic strain in the multi-surface plasticity model [46]. In the numerical simulations, the relation $\tan\phi_r/\tan\phi_0 = 1$ was used.

5.3. Interface constitutive models

The solution to the homogenization problem leads to define the governing stress–strain relationships for the mortar interfaces. In particular, the blue curves in Fig. 13a and b refer to the homogenized behavior in tension for horizontal and vertical interfaces, respectively. Moreover, the blue curves in Fig. 13c and d refer to the interface homogenized behavior in compression and in shear for different value of the compression stress, respectively. In the same figures, the black curves represent the multi-linear approximations used in the numerical simulations [44]. The qualitative constitutive models are reported in Fig. 13e–g for the sake of clarity. In particular, the interface behavior in tension (Fig. 13e) shows an initial elastic branch with cracking strength f_t, followed by a linear softening branch. The interface behavior in compression (Fig. 13f) shows an initial elastic branch up to f_{ce}, a linear hardening branch with crushing strength f_{cp}, and a linear softening branch. Finally, the interface behavior in shear (Fig. 13g) is characterized by linear elastic and softening branches, followed by a horizontal segment corresponding to the residual cohesion. The maximum and residual shear strengths, both depending on the acting compression stress, are given by $\tau_p = c_0 - \sigma\tan\phi$ and $\tau_r = c_{r0} - \sigma\tan\phi_r$, respectively, with c_{r0} being the residual cohesion. Three independent uniaxial damage models were incorporated into the constitutive laws of Fig. 13e–g, leading to unloading and re-loading paths with slope lower than those corresponding to the undamaged material. In particular, the elastic moduli were assumed to deteriorate through the classical relation $K_{dam} = (1 - D_k)K$, with K and $D_k < 1$ being initial modulus and damage parameter, respectively, for tension, compression or shear behavior. The parameters

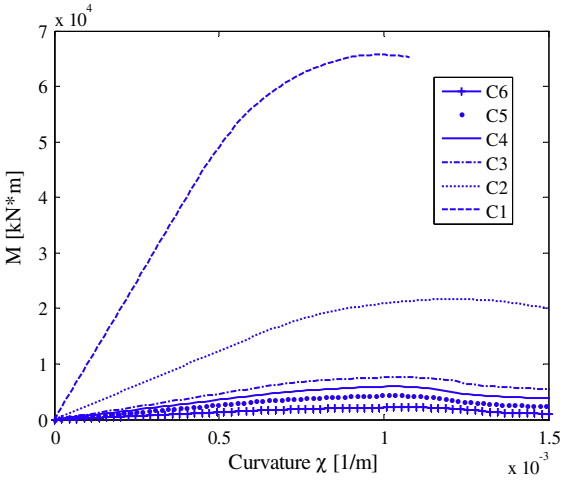

Fig. 14. Moment–curvature relationships for the 6 cross sections of Fig. 11d.

Table 8
Seismic events selected for the RHA.

Event	Label	Year	Magnitude	Duration (s)
Irpinia (Italy)	IR	1980	6.9	85
Niigata (Japan)	NI	2004	6.3	83
Christchurch (New Zealand)	CH	2011	6.2	40
Emilia (Italy)	ER	2012	5.8	40
Emilia (Italy), Casaglia station	CA	2012	5.8	40

of the interface constitutive models used in the RHA are summarized in Table 7. In particular, with regard to the crushing strength, the value $f_{cp} = 3.5$ MPa was adopted as in the pushover analyses.

5.4. Beam model

Because of their relatively reduced computational effort, the numerical models using beam finite elements are the most common tools for the RHA of structures. With regard to slender masonry structures, both linear elastic beam elements connected by means of nonlinear joints [47] and nonlinear beam elements characterized by a smeared cracking model with exponential tension softening and constant shear retention [11] were used in the literature. In the present paper, a beam model of the chimney was implemented in STRAND7 [21] using 21 two-node beam elements (Fig. 11e). To reproduce the cyclic behavior of the structure, a modified Takeda hysteretic law [48] was assigned to the elements (see also [49]). Moreover, bending moment–curvature relationships suitable for the beam-element cross sections were defined using the solution to the homogenization problem for tension and compression modes (Fig. 14). The mechanical properties adopted for tension and compression behavior of the beam model were the same as for the 2D model (Table 7). Anyway, the beam models do not allow for taking possible shear failure modes of masonry into due account.

Table 7
Material properties defining the interface constitutive laws of Fig. 13e–g used for the RHA with the 2D model. Tension and compression properties were also adopted for the RHA with the beam model.

Young's modulus	Tension		Compression				Shear			
E (MPa)	f_t (MPa)	ε_u	f_{ce} (MPa)	f_{cp} (MPa)	ε_p	ε_u	G (MPa)	c_0 (MPa)	$\phi = \phi_r$	c_r
1500	0.1	$7.5\varepsilon_e$	3.0	3.5	$3.0\varepsilon_e$	$4.5\varepsilon_e$	660	0.1	30°	0

5.5. Input ground motions

The axial symmetry of the chimney allow for the use of a single component of the horizontal ground motion. Five couples of horizontal and vertical real acceleration records were used for the RHA of the model with two-dimensional finite elements. Year of occurrence, magnitude and recording duration of the seismic events, along with the labels used in the following to identify them, are reported in Table 8. Four of these couples, scaled to obtain compatibility with horizontal and vertical elastic response spectra provided by [19] for use class II and ground type C, were selected using REXEL [50]. In particular, the fourth couple corresponds to the second main shock of Emilia earthquake, and was recorded in proximity of the epicenter, about 40 km far from Ferrara. Because of the relative position of Ferrara with respect to the epicenter (Fig. 2), the horizontal component of interest was assumed to be that with east–west orientation. Finally, the fifth couple of accelerograms, corresponding to the same event as the fourth, was recorded by the station located in Casaglia, about 5 km far from Ferrara in the direction of the epicenter, and was used in the simulations without scaling. Even in this case, the horizontal component was east–west oriented. With regard to the beam model, only the horizontal components of the seismic events of Table 8 were used.

5.6. Numerical results

The response histories in term of lateral displacement for a node located on the top of the chimney are reported in Fig. 15a and b for the 2D and the beam models, respectively. The four spectrum-compatible accelerograms obtained from IR, NI, CH and ER earthquakes gave rise, for the two models, to almost the same mean value of the residual displacement, i.e. 0.17 m for the 2D model and 0.18 m for the beam model. Nevertheless, the standard deviation of the residual displacement obtained from the 2D model, equal to approximately 0.02 m, is only 37% of that obtained from the beam model. The maximum residual displacement correspond to NI earthquake for the 2D model and to CH earthquake for the beam model. The residual displacement predicted by the 2D model for CA earthquake, equal to approximately 0.05 m, is close to the out-of-straightness of 0.06 m measured after Emilia earthquake's main shocks with 3D laser scanning technique. Conversely, the beam model underestimates the residual displacement produced by CA earthquake by 67%. The inability of the beam

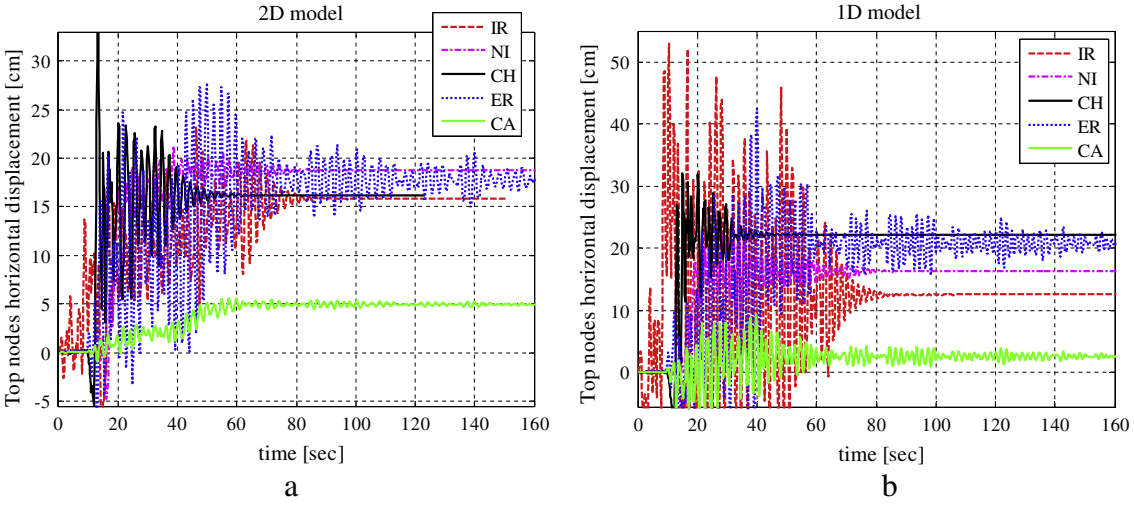

Fig. 15. RHA results for the five seismic events of Table 8: displacement time-histories for a node located on the top of the chimney obtained from (a) the 2D model and (b) the beam model.

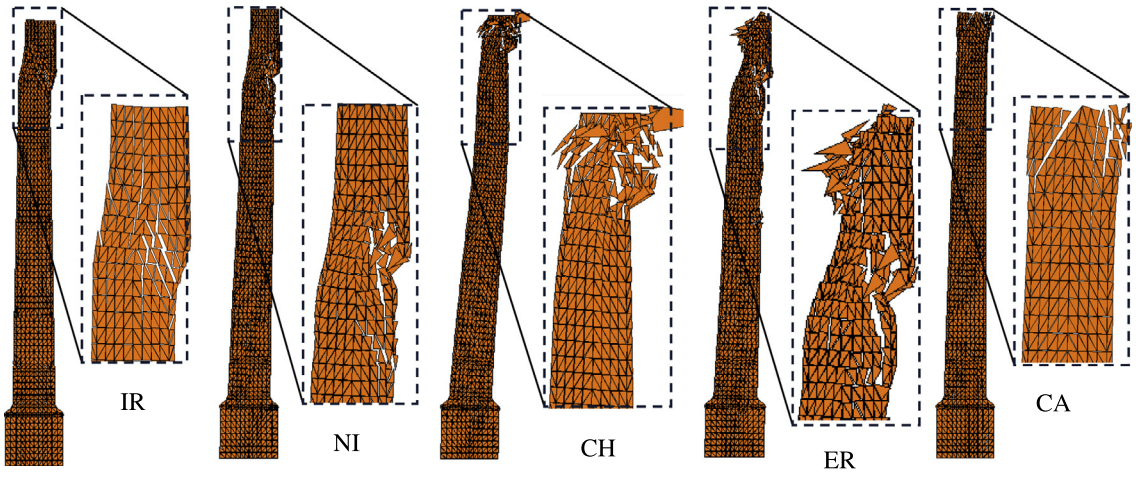

Fig. 16. Deformed shapes of the chimney at the end of the simulations for the model with rigid triangular elements and nonlinear interfaces. Global view and detail of the upper part of the structure for the five seismic events of Table 8.

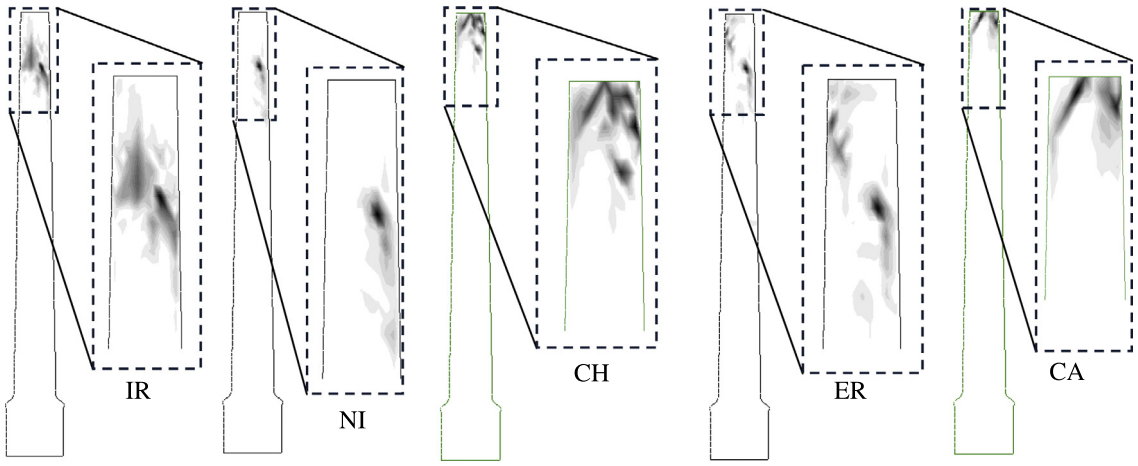

Fig. 17. Damage in shear at the end of the simulations for the model with rigid triangular elements and nonlinear interfaces. Global view and detail of the upper part of the structure for the five seismic events of Table 8.

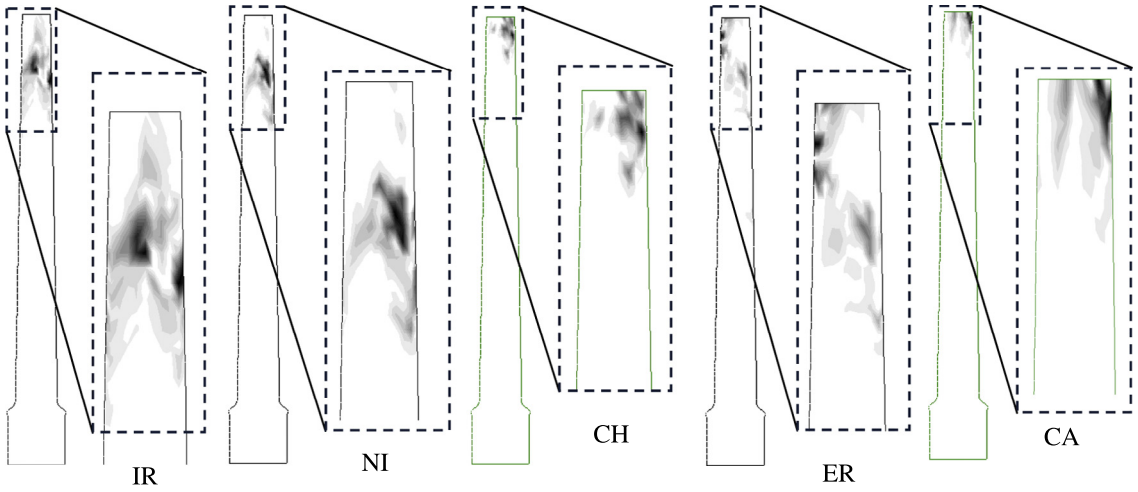

Fig. 18. Damage in compression at the end of the simulations for the model with rigid triangular elements and nonlinear interfaces. Global view and detail of the upper part of the structure for the five seismic events of Table 8.

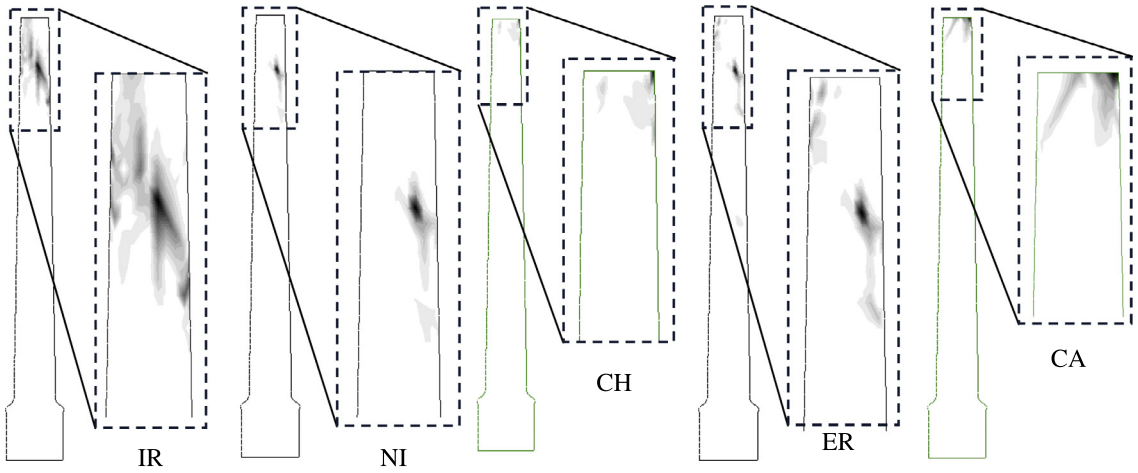

Fig. 19. Damage in tension at the end of the simulations for the model with rigid triangular elements and nonlinear interfaces. Global view and detail of the upper part of the structure for the five seismic events of Table 8.

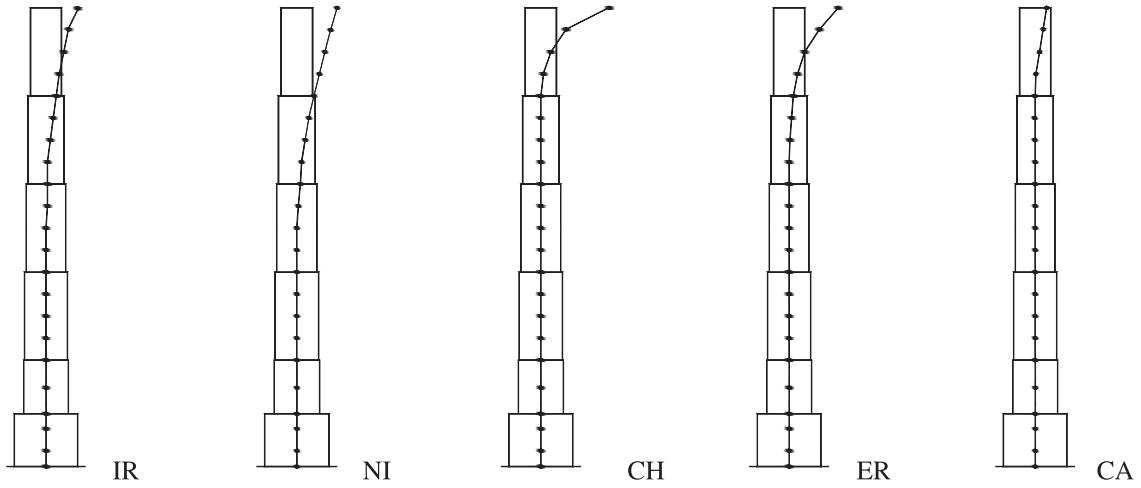

Fig. 20. Deformed shapes of the chimney at the end of the simulations for the model with nonlinear beam elements: lateral displacements of the centroidal axis of the structure for the five seismic events of Table 8.

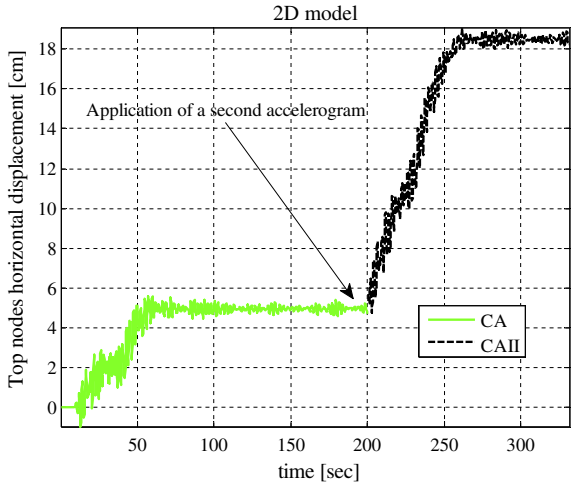

Fig. 21. Top horizontal displacement time history obtained by applying to the 2D model two equal CA accelerograms (CA and CAII) in succession.

model of predicting possible shear failure mechanisms can explain the discrepancy between the two models only partially. It is believed that another important source of difference lies in the effect of the vertical component of the ground motion, that was taken into account in the 2D model, but was ignored in the beam model. In fact, this component was relatively much more important for nonscaled CA earthquake than for all other spectrum-compatible earthquakes. It is worth underlining that the vertical component of the ground motion leads to increased second-order effects when acts downward and may be detrimental for the friction-dependent component of the shear resistance when acts upward. The deformed shapes at the end of the simulations using the 2D model are reported in Fig. 16. They systematically show a collapse mode of the upper part of the structure ($z = 42$–50 m), associated with the formation of diagonal cracks. Depending on the specific accelerogram applied, the portion of the structure involved by severe damage is more or less pronounced. This appears to be a typical behavior linked with the peculiar characteristics of the signal in comparison with the natural frequencies of the structure. The analysis using CA ground motion put in evidence the formation of cracks starting from the section at $z = 46.5$ m, quite close to the altitude of the observed cracks (Fig. 3a and b). The origin of the cracks is clarified by the damage patterns shown in Figs. 17–19, referred to shear, compression and tension failure modes, respectively. In particular, the diagonal cracks appear to be triggered by a prevailing shear failure mode (Fig. 17), locally

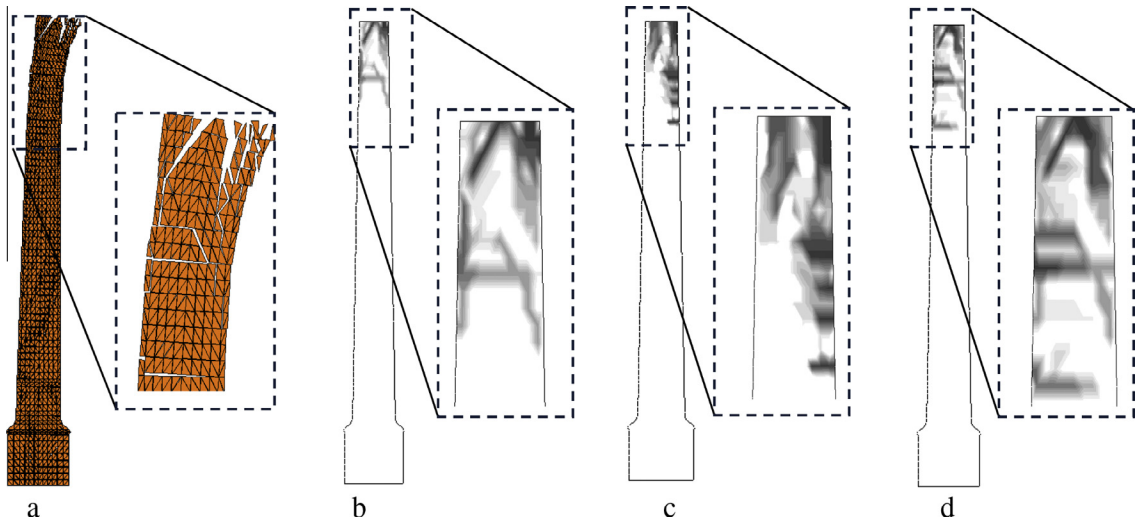

Fig. 22. Damage level attained after the second CA earthquake (CAII): (a) final deformed shape, and damage in (b) shear, (c) compression, and (d) tension.

associated with masonry crushing (Fig. 18) and sometimes combined with the tension mode (Fig. 19).

The beam model (Fig. 20) shows a collapse mode of the intermediate/upper part of the chimney (z = 28–50 m), ruled, as expected, by dominantly flexural plastic hinges which rarely occur in practice.

Finally, the seismic response of the damaged structure was assessed using the 2D model. In particular, at the end of the response history obtained for CA earthquake, a second CA earthquake (CAII) was applied to the chimney. This new analysis, accounting for the damages occurred during the first ground motion, was aimed at investigating the effects of another ground motion of equal intensity. The results in terms of top horizontal displacement are reported in Fig. 21, where the green curve, already shown in Fig. 15a, and the black curve refer to the first and second CA earthquakes, respectively. During CAII ground motion, the influence of the current damage level is significant, leading the horizontal displacement to increase almost linearly up to a new residual displacement equal to approximately 0.2 m. The final deformed shape and the damage maps associated with shear, compression and tension behavior are reported in Fig. 22, showing a strong deterioration with respect to the damage level shown in Figs. 16–19 for the first CA earthquake. In particular, the shear failure mode highlighted by the first ground motion, seems to trigger, during the second earthquake, an overturning mode of the upper part of the chimney (Fig. 22a), with three evident horizontal cracks on the tension side (Fig. 22d) and crushing of masonry on the compression side (Fig. 22c).

6. Conclusions

A 50 m-high masonry chimney damaged by the 2012 Emilia earthquake was analyzed using static and dynamic analysis techniques. With regard to the static analyses, the lateral force method yielded an unrealistically high vulnerability to overturning at z = 11 m. This failure mode was confirmed by the pushover analyses using traditional force distributions. Conversely, response spectrum method (RSM) and modal pushover analysis (MPA) including up to six modes led to a shear failure mechanism for $z \geqslant 42$ m that substantially complies with the observed damages. These analyses confirmed that considering all modes with effective modal mass larger or equal to approximately 5% is essential to reproduce the seismic response of tall structures. The behavior factor q = 1.1 estimated from the MPA indicates a very low dissipative capacity. In these conditions, the MPA tends to coincide with the RSM, which seems then to be a reasonable analysis tool for the fast vulnerability assessment of the meaningful case study presented.

With regard to the dynamic analyses, a 2D model of the chimney was developed using three-node rigid elements connected by means of nonlinear interfaces. The responses to four spectrum-compatible accelerograms confirmed that the shear failure mechanism is generally crucial for the cross sections at $z \geqslant 42$ m. Moreover, the response to the ground motion recorded during the second Emilia earthquake's main shock indicates a significant influence of the vertical seismic component and was shown to be characterized by a damage pattern and a residual lateral displacement very close to those observed. For the same ground motion, the response history analysis with a more simple beam model predicted a dominantly flexural failure mechanism for $z \geqslant 43$ m, that does not comply with the observed damages. To investigate the effects due to a new seismic event on the earthquake-damaged structure, the 2D model was subjected to two equal ground motions corresponding to the second Emilia earthquake's main shock applied in succession. The analysis highlighted the formation of three horizontal cracks on the tension side of the upper part of the chimney, associated with crushing of masonry on the compression side.

The mechanical survey conducted after the Emilia sequence undoubtedly is incomplete and an in situ characterization of the material properties has already been planned for the near future, together with an accurate calibration of soil-structure interaction parameters through procedures of dynamic identification. Further analyses should probably include the effects of the torsional modes of vibration of the chimney, neglected in this study. In order to rapidly reopen the buildings in the surrounding area, the upper, damaged 10 m of the chimney were recently disassembled for security reasons in view of the next reassembling.

Acknowledgements

The present investigation was developed within the activities of the (Italian) University Network of Seismic Engineering Laboratories – ReLUIS in the research program funded by the Italian Civil Protection National Service – Progetto Esecutivo 2010–2013 – Research Line 1. Financial support of the University of Ferrara is gratefully acknowledged.

References

[1] Magliulo G, Ercolino M, Petrone C, Coppola O, Manfredi G. Emilia earthquake: the seismic performance of precast RC buildings. Earthq Spectra 2013. http://dx.doi.org/10.1193/091012EQS285M.
[2] Cattari S, Degli Abbati S, Ferretti D, Lagomarsino S, Ottonelli D, Tralli A. Damage assessment of fortresses after the 2012 Emilia earthquake (Italy). Bull Earthq Eng 2012;2013. http://dx.doi.org/10.1007/s10518-013-9520-x.
[3] Huang W, Gould PL, Martinez R, Johnson GS. Non-linear analysis of a collapsed reinforced concrete chimney. Earthq Eng Struct Dynam 2004;33(4):485–98. http://dx.doi.org/10.1002/eqe.362.
[4] Huang W, Gould PL. 3-D pushover analysis of a collapsed reinforced concrete chimney. Finite Elem Anal Des 2007;43(11–12):879–87. http://dx.doi.org/10.1016/j.finel.2007.05.005.
[5] Pallarés FJ, Ivorra S, Pallarés L, Adam JM. State of the art of industrial masonry chimneys: a review from construction to strengthening. Constr Build Mater 2011;25(12):4351–61. http://dx.doi.org/10.1016/j.conbuildmat.2011.02.004.
[6] Riva G, Zorgno AM. Old brickwork chimneys: structural features and restoration problems. In: Brebbia CA, Leftheris B, editors. Structural studies, repairs, and maintenance of historical buildings IV: dynamics, repairs and restoration. Transactions on the built environment, vol. 2. Southampton: WIT Press; 1995. vol. 15. http://dx.doi.org/10.2495/STR950362.
[7] Pistone G, Riva G, Zorgno AM. Structural behaviour of ancient chimneys. In: Brebbia CA, Sanchez-Beitia S, editors. Structural studies, repairs, and maintenance of historical buildings. Transactions on the built environment, vol. 26. Southampton: WIT Press; 1997. http://dx.doi.org/10.2495/STR970321.
[8] Ghobarah A, Baumer T. Seismic response and retrofit of industrial brick masonry chimneys. Can J Civ Eng 1992;19(1):117–28. http://dx.doi.org/10.1139/l92-012.
[9] Pallarés FJ, Aguero A, Martin M. Seismic behaviour of industrial masonry chimneys. Int J Solids Struct 2006;43(7–8):2076–90. http://dx.doi.org/10.1016/j.ijsolstr.2005.06.014.
[10] Pallarés FJ, Aguero A, Ivorra S. A comparison of different failure criteria in a numerical seismic assessment of an industrial brickwork chimney. Mater Struct 2009;42(2):213–26. http://dx.doi.org/10.1617/s11527-008-9379-5.
[11] Peña F, Lourenço PB, Mendes N, Oliveira DV. Numerical models for the seismic assessment of an old masonry tower. Eng Struct 2010;32(5):1466–78. http://dx.doi.org/10.1016/j.engstruct.2010.01.027.
[12] Aoki T, Sabia D. Structural characterization of a brick chimney by experimental tests and numerical model updating. Masonry Int 2006;19:41–52.
[13] Aoki T, Sabia D, Rivella D. Influence of experimental data and FE model on updating results of a brick chimney. Adv Eng Softw 2008;39(4):327–35. http://dx.doi.org/10.1016/j.advengsoft.2007.01.005.
[14] Pallarés FJ, Ivorra S, Pallarés L, Adam JM. Seismic assessment of a CFRP-strengthened masonry chimney. Struct Build 2009;162(5):291–9. http://dx.doi.org/10.1680/stbu.2009.162.5.291.
[15] Google Earth (Version 7.1.2.2041) [Software]. Emilia-Romagna 44.571469°N, 11.225741°W, elevation 93M. Borders and labels, and water bodies data layers. Google Inc.: Mountain View, 2013. <http://www.filehippo.com/it/download_google_earth>.
[16] Chopra AK, Goel RK. A modal pushover analysis procedure for estimating seismic demands for buildings. Earthq Eng Struct Dynam 2002;31(3):561–82. http://dx.doi.org/10.1002/eqe.144.
[17] European Committee for Standardization. EN 772-1:2011. Methods of tests for masonry units. Part 1: determination of compressive strength. Brussels, Belgium; 2011.

[18] European Committee for Standardization. EN 1996-1-1:2005. Eurocode 6 – design of masonry structures – part 1-1: general rules for reinforced and unreinforced masonry structures. Brussels, Belgium; 2005.
[19] Italian Ministry of Infrastructure and Transport. Italian building code-D.M. 14/01/2008. Rome, Italy; 2008 [in Italian].
[20] European Committee for Standardization. EN 1998-3:2005. Eurocode 8 – design of structures for earthquake resistance – part 3: assessment and retrofitting of buildings. Brussels, Belgium; 2005.
[21] STRAND7®. Theoretical manual – theoretical background to the Strand7 finite element analysis system, 1st ed. Strand7 Pty Ltd., Sidney; 2005.
[22] Minghini F, Tullini N, Laudiero F. Locking-free finite elements for shear deformable orthotropic thin-walled beams. Int J Numer Meth Eng 2007;72(7):808–34. http://dx.doi.org/10.1002/nme.2034.
[23] Chopra AK. Dynamics of structures. Theory and applications to earthquake engineering. 2nd ed. Upper Saddle River: Prentice Hall; 2001.
[24] Halabian AM, El Naggar MH. Effect of non-linear soil-structure interaction on seismic response of tall slender structures. Soil Dynam Earthq Eng 2002;22(8):639–58. http://dx.doi.org/10.1016/S0267-7261(02)00061-1.
[25] Michel C, Gueguen P, Lestuzzi P. Observed non-linear soil-structure interaction from low amplitude earthquakes and forced-vibration recordings. In: Proceedings of the 8th international conference on structural dynamics (Eurodyn 2011), Leuven, 2011, July 4–6.
[26] Gazetas G. Analysis of machine foundation vibrations: state of the art. Soil Dynam Earthq Eng 1983;2(1):2–42. http://dx.doi.org/10.1016/0261-7277(83)90025-6.
[27] Pais A, Kausel E. Approximate formulas for dynamic stiffnesses of rigid foundation. Soil Dynam Earthq Eng 1988;7(4):213–27. http://dx.doi.org/10.1016/S0267-7261(88)80005-8.
[28] Directive of the President of the Council of Ministers of Italy. Assessment and reduction of the seismic risk of the cultural heritage with reference to the Italian building code-DPCM 09/02/2011. Rome, Italy; 2011 [in Italian].
[29] European Committee for Standardization. EN 1998-1:2004. Eurocode 8 – design of structures for earthquake resistance – part 1: general rules, seismic actions and rules for buildings. Brussels, Belgium; 2004.
[30] DIANA Finite Element Analysis, Release 9.3. User's manual. TNO DIANA BV, Delft; 2009.
[31] Rots JG, Blaauwendraad J. Crack models for concrete: discrete or smeared? Fixed, multi-directional or rotating? HERON J 1989;34(1):1–59.
[32] Milani G, Casolo S, Naliato A, Tralli A. Seismic assessment of a medieval masonry tower in Northern Italy by limit, non-linear static and full dynamic analyses. Int J Architect Herit: Conserv Anal Restor 2012;6(5):489–524. http://dx.doi.org/10.1080/15583058.2011.588987.
[33] Colajanni P, Potenzone B. Two proposals for the force distributions used in the pushover analysis. In: Cosenza E, Manfredi G, Monti G, editors. Evaluation and reduction of the seismic vulnerability of reinforced concrete buildings. Monza: Polimetrica International Scientific Publisher; 2008. p. 241–8 [in Italian].
[34] Goel RK, Chopra AK. Evaluation of modal and FEMA pushover analyses: SAC buildings. Earthq Spectra 2004;20(1):225–54. http://dx.doi.org/10.1193/1.1646390.
[35] Goel RK, Chopra AK. Extension of modal pushover analysis to compute member forces. Earthq Spectra 2005;21(1):125–39. http://dx.doi.org/10.1193/1.1851545.
[36] Reyes JC, Chopra AK. Three-dimensional modal pushover analysis of buildings subjected to two components of ground motion, including its evaluation for tall buildings. Earthq Eng Struct Dynam 2011;40(7):789–806. http://dx.doi.org/10.1002/eqe.1060.
[37] Reyes JC, Chopra AK. Evaluation of three-dimensional modal pushover analysis for unsymmetric-plan buildings subjected to two components of ground motion. Earthq Eng Struct Dynam 2011;40(13):1475–94. http://dx.doi.org/10.1002/eqe.1100.
[38] Antoniou S, Pinho R. Development and verification of a displacement-based adaptive pushover procedure. J Earthq Eng 2004;8(5):643–61. http://dx.doi.org/10.1080/13632460409350504.
[39] Ferracuti B, Pinho R, Savoia M, Francia R. Verification of displacement-based adaptive pushover through multi-ground motion incremental dynamic analyses. Eng Struct 2009;31(8):1789–99. http://dx.doi.org/10.1016/j.engstruct.2009.02.035.
[40] European Committee for Standardization. EN 1998-6:2005. Eurocode 8 – design of structures for earthquake resistance – part 6: towers, masts and chimneys. Brussels, Belgium; 2005.
[41] Lemos J. Discrete element modeling of masonry structures. Int J Architect Herit: Conserv Anal Restor 2007;1(2):190–213. http://dx.doi.org/10.1080/15583050601176868.
[42] Casolo S, Peña F. Rigid element model for in-plane dynamics of masonry walls considering hysteretic behaviour and damage. Earthq Eng Struct Dynam 2007;36(8):1029–48. http://dx.doi.org/10.1002/eqe.670.
[43] Casolo S, Milani G, Uva G, Alessandri C. Comparative seismic vulnerability analysis on ten masonry towers in the coastal Po Valley in Italy. Eng Struct 2013;49:465–90. http://dx.doi.org/10.1016/j.engstruct.2012.11.033.
[44] Milani G. Simple homogenization model for the non-linear analysis of in-plane loaded masonry walls. Comput Struct 2011;89(17–18):1586–601. http://dx.doi.org/10.1016/j.compstruc.2011.05.004.
[45] Milani G, Tralli A. A simple meso-macro model based on SQP for the non-linear analysis of masonry double curvature structures. Int J Solids Struct 2012;49(5):808–34. http://dx.doi.org/10.1016/j.ijsolstr.2011.12.001.
[46] Lourenço PB, Rots JG. Multisurface interface model for analysis of masonry structures. J Eng Mech 1997;123(7):660–8. http://dx.doi.org/10.1061/(ASCE)0733-9399(1997)123:7(660).
[47] Riva P, Perotti F, Guidoboni E, Boschi E. Seismic analysis of the Asinelli Tower and earthquakes in Bologna. Soil Dynam Earthq Eng 1998;17(7–8):525–50. http://dx.doi.org/10.1016/S0267-7261(98)00009-8.
[48] Allahabadi R, Powell GH. Drain-2DX user guide. Report no. UCB/EERC-88/06. College of Engineering, University of California, Berkeley; 1988.
[49] Lestuzzi P, Belmouden Y, Trueb M. Non-linear seismic behavior of structures with limited hysteretic energy dissipation capacity. Bull Earthq Eng 2007;5(4):549–69. http://dx.doi.org/10.1007/s10518-007-9050-5.
[50] Iervolino I, Galasso C, Cosenza E. REXEL: computer aided record selection for code-based seismic structural analysis. Bull Earthq Eng 2010;8(2):339–62. http://dx.doi.org/10.1007/s10518-009-9146-1.